PAPER

CrossMark
click for updates

Structural, electronic and thermoelectric behaviour of CaMnO₃ and CaMnO(₃₋δ)

Marco Molinari,[a] David A. Tompsett,[a] Stephen C. Parker,*[a] Feridoon Azough[b] and Robert Freer[b]

First principle calculations were employed to investigate the orthorhombic perovskite CaMnO₃ and the impact of reduced oxygen content on the electronic, structural and thermoelectric properties. On partial reduction to CaMnO₂.₇₅, oxygen vacancies order in a zig–zag arrangement and a further reduction to CaMnO₂.₅, is predicted to form a brownmillerite-like structure. We found that reduced structures have a large volume expansion which can be related to the formation of domains and cracking in experimental samples. On calculating the thermoelectric properties, we found that the partially reduced structures have more favourable Seebeck coefficients compared to the highly reduced structures. The structures can also be separated into two classes based on the resistivity showing low or high resistance depending on the oxygen vacancies arrangement and content. However none of the intrinsically doped structures shows enhanced power factors and *ZT*.

I.   Introduction

Energy production from current technologies, particularly fossil fuels has a negative impact on the environment and on the human living conditions while global energy consumption increases. The development of alternative sources and the improvement of the energy conversion technologies are therefore desirable. Thermoelectric (TE) devices convert waste heat into electrical energy and can provide supplemental energy.[1,2] TE generation is limited by the low energy conversion efficiency which depends on the design of the device, on the operating temperatures and on the thermoelectric figure of merit of the material, *ZT*. The figure of merit given in eqn (1), is dimensionless and comprises the Seebeck coefficient or thermopower, *S*, the electrical conductivity, σ, the electronic (κ_e) and lattice (κ_l) contributions to the thermal conductivity and the absolute temperature, *T*.

$$ZT = \frac{\sigma S^2}{(\kappa_e + \kappa_l)} T \tag{1}$$

Devices that implement materials with *ZT* > 1 are considered most cost effective. A TE generator comprises alternating series of p- and n-type conducting materials. Thus the TE compatibility factor, $s = |(1 + ZT)^{0.5} - 1|/(ST)$, was introduced to define the conversion efficiency of the generator. To maximize the

efficiency, the *s* values of the n- and p-type materials should be similar within the operating temperature range and their ratio generally <2.[3] Furthermore it is of extreme importance that the *ZT* over the working temperature range of the TE device is constant.

Obtaining a large *ZT* is complicated by three interconnected properties that influence the performance of the material: improvements in one property can be offset by changes in the other properties.[4] Thus three key properties need to be examined for improved efficiency. The Seebeck coefficient should be large as it is related to the voltage generated by the TE material in the temperature gradient, the electrical conductivity should be high to minimize ohmic losses and the thermal conductivity should be low to maintain the thermal gradient.

The largest *ZT* have been achieved with chalcogenites and skutterudites[5,6,7] but their stability at high temperatures and under oxidizing conditions is poor and the toxicity of these compounds is also a major issue. Oxide materials can address these problems and both p- and n-type oxide materials have been exploited for use in thermoelectric devices. However issues with their usage still remain, although for performance they are promising.

Amongst the candidates are layered complex oxides, doped zinc oxide derivatives, and perovskite-type oxides. The major advantage of the perovskites is the flexibility of the doping on either A and B sites covering most of the periodic table, which provides for a broad selection of material–property combinations. Simple perovskites are not strong potential TE materials as they are normally good insulators with high Seebeck coefficients (*S*). However, improvements in the TE properties are achievable through cation substitution.[1,2,8,9]

[a]Department of Chemistry, University of Bath, Claverton Down, Bath BA2 7AY, UK. E-mail: s.c.parker@bath.ac.uk

[b]School of Materials, Material Science Centre, University of Manchester, Manchester M1 7HS, UK

This journal is © The Royal Society of Chemistry 2014

J. Mater. Chem. A, 2014, **2**, 14109–14117 | **14109**

We focus on the n-type perovskite $CaMnO_3$ (CMO). The efficiency of superstructures based on CMO[10–16] has been discussed in the literature but little is known about the effect of oxygen partial pressure on the thermoelectric properties. CMO samples are affected by cracking[17] possibly due to a phase change around 900 °C[15,18] and the inhomogeneity with areas generally rich in oxygen vacancies. However as TE materials can be improved by means of nanostructuring and band engineering, it is of extreme importance to understand the properties of oxygen poor compositions within the sample. CMO gives a perfect case study where the properties of different samples differ broadly depending on the oxygen vacancies ordering. Even though most studies focused on the cubic phase (ref. 19 and references therein), ordering of oxygen vacancies was seen for the orthorhombic phase by Reller.[15,16,20,21]

In the present paper, we first review the structural and magnetic properties of CMO and then assess its thermoelectric properties as a function of the oxygen composition, using first-principles electronic structure simulations and the Boltzmann transport theory.

II. Methodology

The calculation of the self-consistent Hubbard U_{scf} parameter within the PBE-GGA functional for the transition metal Mn, was performed using the Quantum Espresso code[22] using the linear response approach.[23,24] The parameter was calculated for two compositions, $CaMnO_3$ and $CaMnO_{2.75}$. The U_{scf} parameter depends on the configuration and the local coordination but it is accepted to average the values if the environment does not change dramatically. Convergence was reached for a K-points grid of $4 \times 4 \times 4$ and a cut off of 50 Ry. The U_{scf} parameters were 4.14 and 3.84 eV for the pure and the defective structures respectively. Hence the value of 4 eV was chosen, allowing us to reproduce the experimentally determined density of state[25] and the correct stability of the different magnetic phases of CMO.[26] It is worth noting that a U_{eff} of 3 was used in a previous study[26] derived by fitting to HSE results for cubic CMO and later applied to strained orthorhombic CMO successfully.[27]

Geometry optimization was performed using spin-polarized generalized-gradient approximation (GGA) and the projector augmented wave (PAW) approach[28,29] as implemented in the VASP code.[30,31] The exchange correlation functional applied was the PBE[32] with the inclusion of the Hubbard U term using the Liechtenstein[33] approaches ($U = 5$ eV and $J = 1$ eV since the exchange interaction is poorly screened in solids,[34,35] an approach extensively justified in previous work[36,37]). The GGA + U methodology[35] enables the approach to account for the presence of the localized Mn^{3+} states.[38] 3D boundary conditions were used throughout and the cutoff energy for the plane wave basis was 550 eV with the Brillouin zone sampled using a $6 \times 6 \times 6$ Monkhorst–Pack grid to ensure convergence. The larger cutoff of 550 eV, relative to that of 400 eV required for fixed cell calculations, removes the effect of errors due to the Pulay stress during cell relaxation. Relaxation of the structure for all atoms was deemed to have converged when the forces were below

0.01 eV Å^{-1}. Similarly, the lattice vectors were adjusted until all element of the stress tensor was less than 0.05 kbar.

The electronic structures for all the compositions were calculated using the full-potential linearized augmented plane wave besides the local orbitals (L/APW + lo) method as implemented in WIEN2k.[39,40] The exchange correlation functional (PBE) were taken within the GGA + U. The APW + lo method expands the Kohn–Sham orbitals[41] inside the atomic muffin-tin (MT) spheres and plane waves in the interstitial region. The muffin-tin radii were set to 2.09, 1.84 and 1.63 Bohr for Ca, Mn and O respectively. The energy convergence criterion was set to 10^{-5} Ry. For the calculation of transport properties a mesh of 4896 K-points in the irreducible wedge of the Brillouin zone was chosen. The density of states (DOS) was obtained using the tetrahedron method. This application of the all-electron code ensures the high quality of the band structure needed to evaluate the transport properties.

Electronic transport calculations were evaluated by solving the semi-classical Boltzmann transport equation within the relaxation time (τ) and the "rigid band approach" approximation as implemented in the program package BoltzTraP.[42] This approximation allows us to calculate all transport properties with respect to the relaxation time (τ) with the exception of the Seebeck coefficient that can be calculated on an absolute scale. Discussion of the choice of relaxation time will be given in the section v of results.

The lattice component of the thermal conductivity was calculated using the Phonopy code.[43,44] As the calculation is computationally expensive only the lattice thermal conductivity of stoichiometric CMO was evaluated. Atomic displacements of 0.01 Å were employed to obtain the force constants for a single unit cell containing 20 atoms. The numerical calculation was carried out with a $6 \times 6 \times 6$ sampling mesh and a σ value of 0.1 THz. Detailed description of the method can be found in Skelton et al.[44]

It is worth noting that as the materials described here are anisotropic, all of the thermoelectric properties will also show direction dependence. However, as the material synthesised experimentally is polycrystalline and single crystals with homogeneous compositions have not yet been prepared, we report the experimental relevant scalar quantity.[45]

Figures were drawn using the program VESTA.[45]

III. Results and discussion

i. Stoichiometric $CaMnO_3$

CMO adopts the orthorhombic structure with space group Pnma,[46] shown in Fig. 1, from ambient temperature over 1000 K.[47] Tetragonal[15] and rhombohedral phases were also suggested.[18] Properties of pure and doped CMO have been discussed previously.[48,49] CMO shows a G-type antiferromagnetic (AFM) order at T lower than 123 K with the value of the Mn^{4+} moment of 2.65 μ_B.[50] Coexistence of different magnetic orders was reported in $CaMnO_{3-\delta}$ nanoparticles with AFM in the core and ferromagnetism (FM) in the shell.[51] Previous first-principles calculations on $CaMnO_3$ focused both on the cubic phase[26,52–55] and on the orthorhombic phase.[27,56–59]

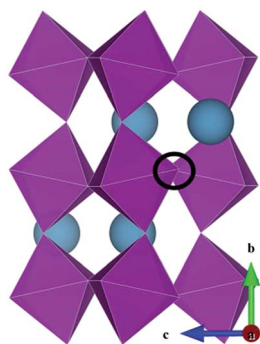**Fig. 1** Perovskite PNMA $CaMnO_3$. Purple octahedra are Mn^{4+}. Ca in teal.

We considered A-, C-, and G-type antiferromagnetic with spin aligned along 010, 101 and 111 directions respectively, and ferromagnetic structures for stoichiometric CMO using the collinear magnetic ordering. All magnetic ordering schemes resulted in insulating structures (charge transfer insulator) with the G-AFM the most stable.[50] Table 1 summarizes the optimized lattice constants, magnetic moment, band gap and energies of different magnetic structures per formula unit with reference to that of G-AFM. The agreement with experiments[25,46,50] and previously reported *ab initio* calculations[55,56,59] is excellent.

ii. Reduced $CaMnO_3$

One of the features of CMO is that it can be readily reduced.[15] $CaMnO_{3-\delta}$ are n-type semiconductors with formation of Mn^{3+} ions upon removal of oxygen. Enthalpy of formation for oxygen vacancies (V_O) was measured to be 1.85 ± 0.07 eV.[60] Tensile strain has been found to lower the formation energy of oxygen vacancies opening routes to engineering vacancy ordering in artificial superstructures.[14–16,27]

Systems with different oxygen vacancies arrangements of reduced CMO were investigated with composition $CaMnO_{2.75}$ and $CaMnO_{2.5}$. We have assumed the structure in a GFM ordering as single crystals of reduced cubic CMO were found to be GFM at low T. Furthermore even though at high T CMO becomes paramagnetic, it was shown that the antiferromagnetic order was an excellent approximation of the actual PM order for UO_2.[61]

Upon relaxation all structures show expansion in volume as experimentally expected.[62] The enthalpy of formation of oxygen

vacancies was calculated following the chemical reaction
$$2Mn_{Mn}^x + O_O^x \rightarrow 2Mn_{Mn}' + V_O^{\cdot\cdot} + \frac{1}{2}O_{2(g)}$$
while the heat of reduction was calculated following the
$$CaMnO_3 \rightarrow CaMnO_{3-\delta} + \frac{\delta}{2}O_{2(g)}[63]$$
with the binding energy of O_2 gas phase molecule in its triplet state (-9.86 eV derived from DFT calculation using a cut off of 50 Ry and a dipole corrections in all directions).

Two structures, displayed in Fig. 2, were considered for the composition $CaMnO_{2.75}$ as there are two inequivalent oxygen positions in within the octahedral coordination of Mn atoms to give rise to significantly different structures. Both configurations have planes of Mn^{3+} but while one has a zig–zag pattern of oxygen vacancies as shown in Fig. 2c, the other one shows a linear arrangement of oxygen vacancies (Fig. 2d). For simplicity we refer to them as zig–zag and line configurations respectively. Mn^{3+} is always in the 5-fold squared pyramidal coordination while Mn^{4+} is in the octahedral coordination. The volume expansions upon reduction are 2.63% and 1.93% for the zig–zag and line configurations respectively. The enthalpies of formation of V_O for zig–zag and line configurations of $CaMnO_{2.75}$ are 2.09 and 2.16 eV respectively while the heats of reduction from stoichiometric $CaMnO_3$ are 0.52 and 0.54 eV respectively.

Different configurations of oxygen vacancies were considered for $CaMnO_{2.5}$. We modelled a brownmillerite-like structure within the stoichiometric unit cell size (Fig. 3a) and a brownmillerite structure for comparison doubling the unit cell along the b direction. A brownmillerite structure can be generated removing at least two oxygen atoms along the <100> direction of a perovskite structure as shown with the circle in Fig. 1; the
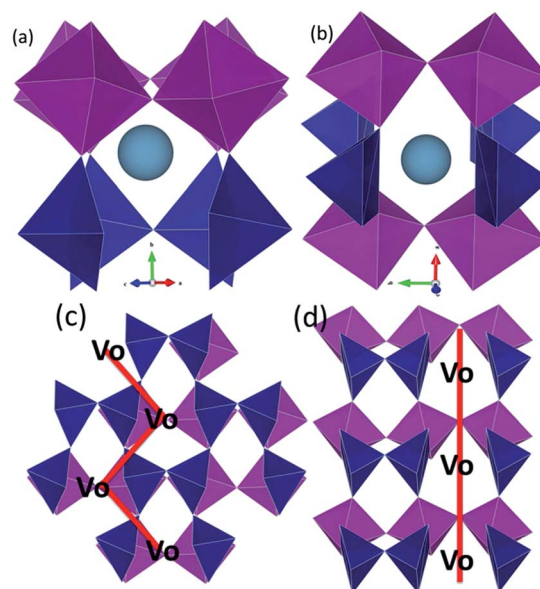
Table 1 Optimized lattice constants (Å), magnetic moment (μ_B), band gap (eV) and energies of the magnetic structures per formula unit with reference to that of G-AFM (eV). Exp. from ref. 25, 46 and 50

	Exp	G	C	A	FM
a	5.282	5.366	5.365	5.377	5.380
b	7.457	7.534	7.545	7.528	7.543
c	5.267	5.313	5.311	5.317	5.316
μ_B	2.65	2.63	2.63	2.67	2.71
E_{gap}	3.07	1.42	1.31	0.98	0.96
ΔE		0.00	0.01	0.03	0.06

Fig. 2 Side views of configurations (a) zig–zag and (b) line for $CaMnO_{2.75}$. Top view of the oxygen vacancy (V_O) arrangements (c) for zig–zag and (d) line configurations. The zig–zag and linear arrangements are shown with red line to help visualization. Purple octahedra and blue squared pyramids are Mn^{4+} and Mn^{3+} respectively. Ca in teal.

This journal is © The Royal Society of Chemistry 2014
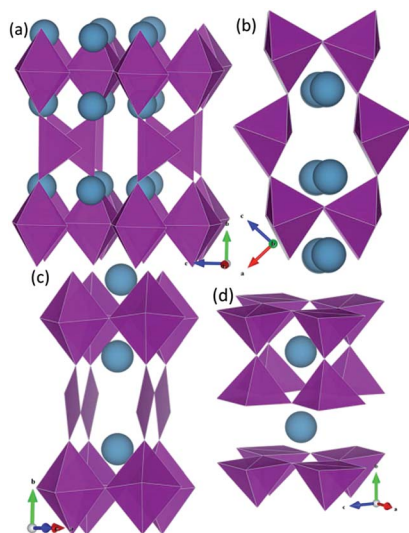
J. Mater. Chem. A, 2014, **2**, 14109–14117 | **14111**

Fig. 3 Configurations (a–d) for CaMnO$_{2.5}$. Polyhedra of Mn in purple. Ca in teal.

octahedral coordination of Mn ion becomes 4-fold and undertakes large relaxation in order to form the tetrahedral coordinated plane. The brownmillerite structure has lines of oxygen vacancies arranged in a simple cubic grid (in the *a* direction), whereas for the brownmillerite-like the oxygen vacancies lines are in a body centred grid. The two structures have however many similarities, both comprising layers of octahedral coordinated Mn^{3+} and layers of 4-fold coordinated Mn^{3+} ions with lines of oxygen vacancies along the a direction and an expansion in the volume of about 6.70%. The enthalpies of formation of V$_O$ were calculated to be 1.50 eV for the brownmillerite-like and 1.57 eV for the brownmillerite structures respectively (the heats of reduction were calculated to be 0.75 and 0.78 eV respectively). The brownmillerite-like structure (Fig. 3a) was also minimized with Mn ions in the oxidation states IV (6-fold coordinated) and II (4-fold coordinated) but the enthalpy of formation of V$_O$ was calculated to be 1.72 eV (the heat of reduction was 0.82 eV) indicating that the mixed oxidation state for Mn gives rise to energetically less stable configurations. In configuration b (Fig. 3b) the oxygen vacancies are arranged in lines along the *b* direction producing a structure where all the Mn^{3+} ions are 5-fold coordinated with a enthalpy of formation of V$_O$ of 1.63 eV (the heat of reduction was 0.82 eV) and a volume expansion of 4.33%. Configuration c (Fig. 3c) has layers of octahedral coordinated Mn^{3+} and layers of squared planar coordinated Mn^{3+} with oxygen vacancy lines along the ac direction. This configuration has the highest enthalpy of formation of V$_O$ of 1.79 eV (heat of reduction of 0.89 eV) and one of the highest volume expansion of 6.64%. Finally, configuration d (Fig. 3d) has an entire layer of oxygen removed in the ac plane and all Mn^{3+} are 5-fold squared pyramidal coordinated. The volume expansion is the smallest from CaMnO$_3$ to this composition of 3.19% and the enthalpy of formation of V$_O$ is 1.76 eV (heat of reduction is 0.88 eV). The two most stable configurations found for CaMnO$_{2.5}$ are the brownmillerite

structures, however as they gave rise to similar transport properties we have selected only the bownmillarite-like and configuration b to be representative of the highly reduced CaMnO$_{2.5}$.

iii. Density of states

The partial density of states (PDOS) of stoichiometric and reduced CMO is displayed in Fig. 4. For the purpose of this section it is not important to show the density of states for all the structures as there are common features depending on the composition not on the structure.

CaMnO$_3$ is an insulator with a measured band gap of 3.07 eV and the electron-band structure close to the Fermi level consisting of Mn d and O p orbitals.[25] Fig. 4a shows these features, however the band gap is largely underestimated (1.42 eV) which is a known issue with the methodology used. Upon partial reduction (Fig. 4c) there are states appearing in the gap which are still dominated by O 2p and Mn 3d. The Mn states are filled and represent the Mn^{3+}. CMO shows insulating behaviour with a band gap of approximately 1.30 eV when fully reduced (Fig. 4b). The Fermi level is still dominated by O 2p and Mn 3d but in this case all Mn atoms are in the oxidation state III.

The density of states is of importance as it gives information on the filled and empty energy levels. Thus, the energy scale of the DOS can be seen as a chemical potential with negative values representing the region of hole doping and positive values the region of electron doping. In Fig. 4 the Fermi energy corresponds to chemical potential of 0 eV which is also the top
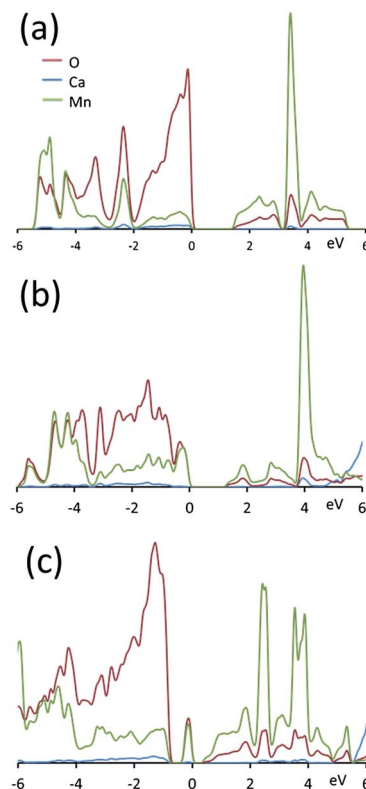

Fig. 4 PDOS on an arbitrary scale of stoichiometric (a), partially reduced (c) and highly reduced (b) CMO. The Fermi energy is at 0 eV.

14112 | *J. Mater. Chem. A*, 2014, **2**, 14109–14117

This journal is © The Royal Society of Chemistry 2014

of the valence band (VB). Stoichiometric and partially reduced CMO can be electron doped showing n-type behaviour. The transport properties were therefore evaluated according to the Boltzmann semiclassical transport theory at values of the chemical potential corresponding to the bottom of the conduction band (CB). For details see ref. 42. At this chemical potential the number of carriers for the studied CMO compositions was found to be of the order of 10^{20} cm^{-3} and the temperature dependency is shown in Fig. 5. Particular consideration has to be drawn for the highly doped CMO containing only Mn in the oxidation state III as it could be treated as an n-type (Mn^{3+} → Mn^{2+}) or p-type (Mn^{3+} → Mn^{4+}). It was reported that Mn$_2$O$_3$ (all Mn^{3+}) and MnO$_2$ (all Mn^{4+}) are respectively p-type and n-type semiconductors.[64] Furthermore Mn$_3$O$_4$ has a p-type behaviour.[65] However, at the best of our knowledge there are no available data to support that highly reduced CMO is a p-type semiconductor. Thus, we calculated the transport properties in correspondence to the bottom of the CB where the material is an n-type semiconductor.

iv. The Seebeck coefficient

The Seebeck coefficients as a function of T are shown in Fig. 6 for all the compositions. These include stoichiometric CMO,
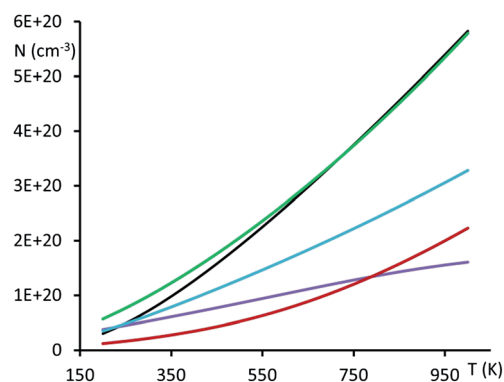

Fig. 5 Number of carrier as evaluated at the bottom of the conduction band as a function of the temperature for all CMO compositions.
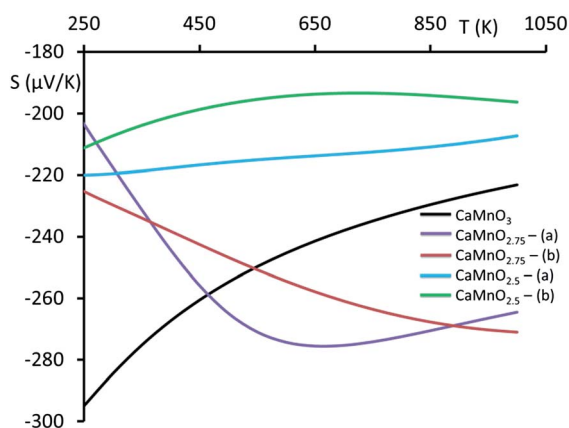

Fig. 6 Seebeck coefficient of stoichiometric and reduce CMO as a function of the temperature.

the two configurations of CaMnO$_{2.75}$ and the two most stable configurations of the highly reduced CaMnO$_{2.5}$ (a and b). The comparison with experiments is not straightforward as the Seebeck depends on the number of carriers which is dependent on the nature of the sample. The values of our calculated S are at the chemical potential corresponding to the bottom of the CB which can be achieved at different carrier concentrations of electrons. Therefore our approach is to describe the differences between the Seebeck coefficients for our structures highlighting those with improved Seebeck to guide possible choices when synthesizing experimental samples. However, discussion of available experimental data is given and where possible, similarities are compared.

The calculated S for CaMnO$_3$ decreases in absolute value as the temperature increases. The same trend is seen for both highly reduced CaMnO$_{2.5}$ configurations with the brownmillerite-like structure performing better than configuration b. However the absolute value is now reduced compared to CaMnO$_3$. In contrast to the stoichiometric and the highly reduced CMO, CaMnO$_{2.75}$ shows an increase of the absolute value of the Seebeck coefficient with the increase in temperature. These trends and values are similar to some of the experimental doped samples.[1] The zig–zag configuration has a higher absolute value of S compared to the structure with lines of oxygen vacancies. This again highlights the importance of defect arrangements. For improved S the best composition is the partially doped CMO with a zig–zag arrangement of oxygen vacancies showing a flat curve in the temperature range between 550 and 850 K. Constant TE properties in the range of operating temperatures are indeed desired.

It is worth noting that our simulations indicate that there are two distinct trends in the variation of the Seebeck coefficient with temperature. The calculations predict that the Seebeck coefficient decreases with increasing temperature for the mixed oxidation states phases (CaMnO$_{2.75}$) while for the stoichiometric and fully reduced phases (comprising only Mn^{4+} or Mn^{3+}) the Seebeck coefficient is predicted to increase with increasing temperature. The Seebeck coefficient is related to the gradient of the density of states at the bottom of the conduction band.[66] In the case of fully oxidised and fully reduced phases the conduction band comes from all of the metal states while in partially reduced phase the metal states are split coming from both Mn^{3+} and Mn^{4+} states. This reduced density will contribute to the change in the gradient of the density of states at the bottom of the conduction band.

The experimental data in the literature show a wide spread of values and different trends. Cohn *et al.* measured the Seebeck coefficient for a single crystal of CMO of -550 μV K^{-1} decreasing to -800 μV K^{-1} in the range of temperature between 300 and 100 K.[67] The value at 300 K is much higher than any of our values at the same temperature. Alfaruq *et al.* measured the S of two polycrystalline CMO (impurities in the samples include CaMnO$_{2.75}$ and CaMn$_2$O$_4$ phases) seeing a sharp reduction in absolute value with increasing temperature to 500 K and reaching a plateau beyond to values of approx. -300 and -170 μV K^{-1} depending on the sample.[68] These values are broadly in the same region of ours. Similarly, Lan *et al.*[69] Xu *et al.*[70] and

Flahaut *et al.*[71] measured the *S* for polycrystalline CMO (likely reduced or containing impurities) decreasing in absolute values with temperature. This is the same trend we see for the stoichiometric and highly reduced CMO. Finally, Liu *et al.* measured the Seebeck coefficient for a polycrystalline CaMnO$_{3-\delta}$ sample[72] decreasing with temperature which is in good agreement with our partially reduced compositions.

It is therefore clear that the large differences between the experimental data is due to the presence of impurities and/or reduced CMO along with extended defects such as grain boundaries in polycrystalline samples. It is worth emphasizing that the simulated structures do not contain any extended defects (grain boundaries).

v. The electronic resistivity

The evaluation of the electronic resistivity is complicated by requiring the relaxation time (τ_0). However, the value of τ_0 only applies a constant shift to all of the resistivity curves for all the compositions studied; *i.e.* leaving the differences between the structures unchanged. Experimental evaluation of the relaxation time is not trivial and a $\tau_0 = 7.5 \times 10^{-14}$ s (ref. 73) was calculated for a polycrystalline film of cubic CMO which is greater than 10^{-15}–10^{-16} s reported in ref. 49 and one order of magnitude greater than $\tau_0 = 4.3 \times 10^{-15}$ s derived for the perovskite SrTiO$_3$.[74] We chose $\tau_0 = 0.5 \times 10^{-16}$ s for all temperatures which brought the resistivity of all our phases in the range of those measured by Loshkareva *et al.*[19] for reduced single crystals of cubic CMO in the range of 150 to 400 K. Fig. 7 shows the corrected data for all the compositions studied as a function of temperature.

Before describing our data, it is worth mentioning that there is a broad spread of experimental data for both single crystal and polycrystalline specimens. This implies that the compositions and the distribution of oxygen vacancies in the grains as well as the grain boundaries have great effect on the measurements. CMO was found to have substantial electronic resistivity at room temperature. 2.7 Ωcm and 1.5 Ωcm were reported for

single crystals[49] and 1 Ωcm for polycrystalline material[73] depending on the concentration and ordering of vacancies. Xu *et al.* also reported a resistivity of approx. 2 Ωcm at 400 K down from 8 Ωcm at room *T*.[70] Flahaut *et al.*[71] reported values of approx. 0.25 Ωcm between 600 and 700 K down from 0.5 Ωcm at room temperature for a polycrystalline material. All these values are broadly in the range of our corrected data, suggesting that the choice of a relaxation time was appropriate. Thus we infer that our data can be used to discriminate between different compositions and most importantly between different arrangements of oxygen vacancies.

We can divide our structures into two groups. The "high resistance" group includes the partially reduced configuration with lines of oxygen vacancies and the highly reduced brownmillerite-like structure while the "low resistance" group comprises the highly reduced b structure (seen by Reller[15] Fig. 5) along with the most stable partially reduced zig–zag configuration. We now attempt to compare these groups with the single crystal samples of cubic reduced CMO of Loshkareva *et al.*[19] In their work the samples with higher resistivity had a composition ranging from CaMnO$_{2.80}$ to CaMnO$_{2.75}$. Considering that the brownmillerite-like structure has never been reported, therefore despite being thermodynamically the most stable structure it might be kinetically not accessible, we suggest that one possible arrangement of oxygen vacancies in their sample was alike the simulated partially reduced configuration with lines of oxygen vacancies. Furthermore, their "low resistance" sample, which shows resistivity values comparable to our highly reduced b structure and partially reduced zig–zag configuration, was supposed to have possibly a higher concentration of oxygen vacancies and less ordered arrangement, which is in agreement with our two simulated structures. While we recognize that the choice of relaxation time shifted our data in the range of Loshkareva *et al.*,[19] it is remarkable how this choice has brought our data broadly close to most of the available experimental data and most importantly gives a possible interpretation of the experimental data in "low" and "high resistance" samples.

From our data we have also calculated the activation energy for electron from $\sigma = (\sigma_0/T) \exp(-E_a/K_bT)$ to be 0.07–0.08 eV for all the compositions. However this is lower compared to the experimental vales of 0.16 and 0.22 eV.[69,75] The difference can be ascribed to the presence of impurities and to the nature of the polycrystalline sample used for the measurement.

vi. The power factor

Fig. 8 shows the power factor ($S^2 \sigma$) as a function of *T*. Lan *et al.*[69] reported values of approx. 0.06 μW cm^{-1} K^{-2} below 750 K and a sharp raise above 800 K up to 0.5 μW cm^{-1}K^{-2} at approximately 1000 K. All our data are in within this range. However there is a broad range of experimental data. Ohtaki *et al.*[75] measured approximately 0.2 and 0.8 μW cm^{-1} K^{-2} at 200 and 700 K respectively while Alfaruq *et al.*[68] reported values of 0.085–0.065 μW cm^{-1} K^{-2} at 1000 K which are one order of magnitude lower then Lan *et al.* Again we must be cautious with direct comparison with experimental data from polycrystalline materials. Our data show that the stoichiometric CMO has the highest PF due
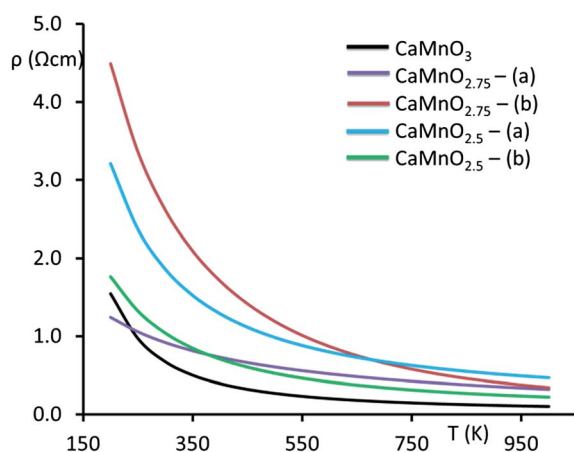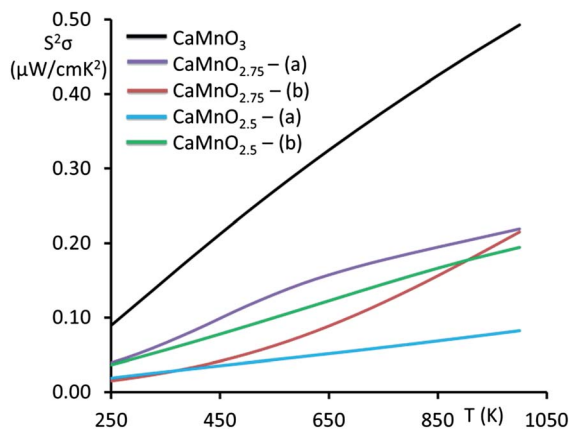

Fig. 7 Electrical resistivity of stoichiometric and reduce CMO as a function of the temperature calculated using a relaxation time of 0.5×10^{-16} s.

Fig. 8 Power factor of stoichiometric and reduce CMO as a function of the temperature calculated using a relaxation time of 0.5×10^{-16} s.

to the high S and the low resistivity (due to the high concentration of carriers as shown in Fig. 5) while the brownmillerite-like structure has the lowest due to a combination of low S and high resistivity. The remaining structures have comparable values. The partially reduced configuration with lines of oxygen vacancies has an acceptable PF due to the high S despite showing the highest resistivity. The highest power factor is shown by the partially reduced composition with zig–zag arrangement of oxygen vacancies due to a high S and low resistivity.

vii. The figure of merit

The figure of merit (ZT) can be calculated as in eqn (1); however before describing our results we detail our approximation in order to calculate the denominator.

The thermal conductivity ($k = k_l + k_e$) is the sum of the electronic component k_e (calculated with a relaxation time of 0.5×10^{-16} s) and the lattice component k_l. As the former is negligible compared to the latter (several order of magnitude), k is mainly assigned to the lattice contribution. The electronic contribution was calculated using the BoltzTraP code while the lattice contribution with the Phonopy code as detailed in the methodology. The calculation of k_l is extremely computationally expensive and therefore was performed only on the stoichiometric CMO. The calculated values as a function of temperature (Fig. 9) are extremely close to the experimental values of Flahaut et al.,[71] Ohtaki et al.[75] and Xu et al.[70] who measured a decrease in the value of k with increasing T.

Therefore we have used the thermal conductivity calculated of the stoichiometric sample for all the structures. This is clearly an approximation as the presence of defects influences the thermal conductivity. Fig. 10 shows the ZT as a function of the temperature.

ZT show the same trend as the PF with the stoichiometric CMO showing the highest and the highly reduced brownmillerite-like structure the lowest achievable figure of merit.
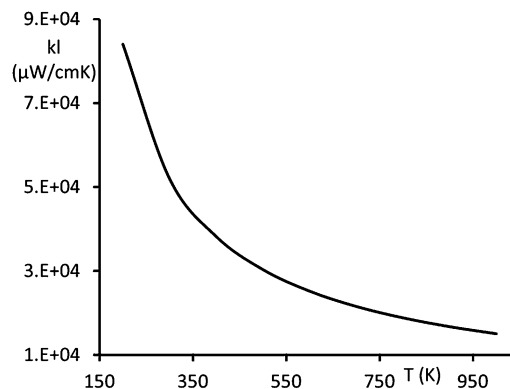

Fig. 9 Lattice thermal conductivity ($\mu W\ cm^{-1}\ K^{-1}$) of stoichiometric and reduce CMO as a function of the temperature.
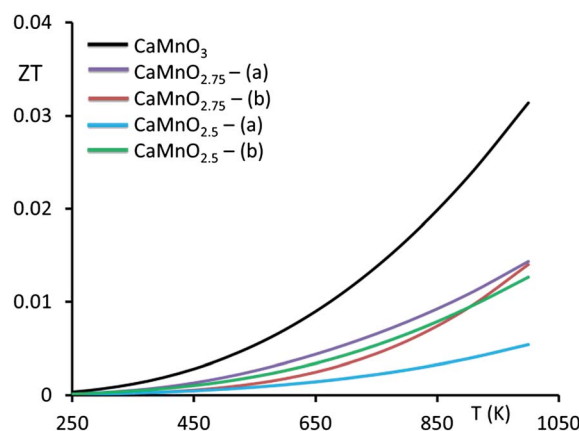

Fig. 10 Figure of merit of the stoichiometric and reduce CMO as a function of the temperature.

The experimental values of Flahaut et al.[71] are significantly higher than ours with a ZT lower than 0.01 and higher that 0.04 at 350 and 950 K respectively.

IV. Conclusions

As perovskite oxides are promising TE materials we have investigated local structures of a candidate material $CaMnO_3$, which shows inhomogeneity with areas generally rich in oxygen vacancies and cracking. In order to model this material we have applied DFT to the structures of different compositions of $CaMnO_{3-\delta}$. The thermodynamically most stable partially reduced configuration does not show ordered lines of oxygen vacancies while the most stable highly reduced structure is a brownmillerite-like which also shows the highest volume expansion. All these structures show volume expansion which suggest that the formation of domains within the material would be responsible for the cracking observed. The brownmillerite-like structure has never been reported experimentally and thus we infer that despite being thermodynamically the most stable it might not be kinetically accessible. We then evaluated the transport properties of these structures to

examine the different impact on the thermoelectric behaviour of CMO samples. Unlike the stoichiometric and fully reduced phases, the partially reduced structures show the Seebeck coefficient to increase (in absolute value) with increasing the temperature. This might be due to the presence of mixed oxidation states which is likely to influence the gradient of the density of states at the bottom of the conduction band. Indeed, this feature might be a general phenomenon in phases with mixed oxidation states which is worthy of further investigation. We found that the partially reduced structure has the highest Seebeck coefficient. However, the ordering of oxygen vacancies in lines increases the resistivity of the structure but as the S is high the power factor ($S^2\sigma$) is still comparable to the partially reduced (zig–zag) structure with lower ordering of oxygen vacancies. We found that there are three structures with comparable power factor and figure of merit which comes out of an inter-play of thermoelectric properties. These two properties are however not constant in a large range of temperature as desirable from an ideal thermoelectric material. The results suggest that although these local structures with enriched ordering of oxygen vacancies might be of importance for other applications they are undesirable for thermoelectric applications of doped CMO samples.

Acknowledgements

References

1 J. W. Fergus, *J. Eur. Ceram. Soc.*, 2012, **32**, 525–540.

2 K. Koumoto, R. Funahashi, E. Guilmeau, Y. Miyazaki, A. Weidenkaff, Y. Wang and C. Wan, *J. Am. Ceram. Soc.*, 2013, **96**, 1–23.

3 G. J. Snyder, *Appl. Phys. Lett.*, 2004, **84**, 2436–2438.

4 J. P. Doumerc, M. Blangero, M. Pollet, D. Carlier, J. Darriet, R. Berthelot, C. Delmas and R. Decourt, *J. Electron. Mater.*, 2009, **38**, 1078–1082.

5 J. Yang and F. R. Stabler, *J. Electron. Mater.*, 2009, **38**, 1245–1251.

6 E. S. Toberer, A. F. May and G. J. Snyder, *Chem. Mater.*, 2010, **22**, 624–634.

7 M. G. Kanatzidis, *Chem. Mater.*, 2010, **22**, 648–659.

8 A. Maignan, S. Hebert, L. Pi, D. Pelloquin, C. Martin, C. Michel, M. Hervieu and B. Raveau, *Cryst. Eng.*, 2002, **5**, 365–382.

9 L. Bocher, M. H. Aguirre, R. Robert, D. Logvinovich, S. Bakardjieva, J. Hejtmanek and A. Weidenkaff, *Acta Mater.*, 2009, **57**, 5667–5680.

10 C. Cardoso, R. P. Borges, T. Gasche and M. Godinho, *J. Phys.: Condens. Matter*, 2008, **20**, 035202.

11 Y. Miyazaki, D. Abe and T. Kajitani, in *Proceedings Ict 07: Twenty-Sixth International Conference on Thermoelectrics*, ed. I. Kim, IEEE, New York, 2008, pp. 129–133.

12 F. Kawashima, X. Y. Huang, K. Hayashi, Y. Miyazaki and T. Kajitani, *J. Electron. Mater.*, 2009, **38**, 1159–1162.

13 K. S. Takahashi, M. Kawasaki and Y. Tokura, *Appl. Phys. Lett.*, 2001, **79**, 1324–1326.

14 I. D. Fawcett, J. E. Sunstrom, M. Greenblatt, M. Croft and K. V. Ramanujachary, *Chem. Mater.*, 1998, **10**, 3643–3651.

15 A. Reller, J. M. Thomas, D. A. Jefferson and M. K. Uppal, *Proc. R. Soc. London, Ser. A*, 1984, **394**, 223–241.

16 A. V. Petrov, S. C. Parker and A. Reller, *Phase Transitions*, 1995, **55**, 229–244.

17 A. Kosuga, S. Urata, K. Kurosaki, S. Yamanaka and R. Funahashi, *Jpn. J. Appl. Phys.*, 2008, **47**, 6399–6403.

18 J. A. Souza, J. J. Neumeier, R. K. Bollinger, B. McGuire, C. A. M. dos Santos and H. Terashita, *Phys. Rev. B: Condens. Matter Mater. Phys.*, 2007, **76**, 024407.

19 N. N. Loshkareva, N. V. Mushnikov, A. V. Korolyov, E. A. Neifeld and A. M. Balbashov, *Phys. Rev. B: Condens. Matter Mater. Phys.*, 2008, **77**, 052406.

20 A. Reller, D. A. Jefferson, J. M. Thomas, R. A. Beyerlein and K. R. Poeppelmeier, *J. Chem. Soc., Chem. Commun.*, 1982, 1378–1380.

21 A. Reller, D. A. Jefferson, J. M. Thomas and M. K. Uppal, *J. Phys. Chem.*, 1983, **87**, 913–914.

22 P. Giannozzi, S. Baroni, N. Bonini, M. Calandra, R. Car, C. Cavazzoni, D. Ceresoli, G. L. Chiarotti, M. Cococcioni, I. Dabo, A. Dal Corso, S. de Gironcoli, S. Fabris, G. Fratesi, R. Gebauer, U. Gerstmann, C. Gougoussis, A. Kokalj, M. Lazzeri, L. Martin-Samos, N. Marzari, F. Mauri, R. Mazzarello, S. Paolini, A. Pasquarello, L. Paulatto, C. Sbraccia, S. Scandolo, G. Sclauzero, A. P. Seitsonen, A. Smogunov, P. Umari and R. M. Wentzcovitch, *J. Phys.: Condens. Matter*, 2009, **21**, 395502.

23 M. Cococcioni and S. de Gironcoli, *Phys. Rev. B: Condens. Matter Mater. Phys.*, 2005, **71**, 035105.

24 H. J. Kulik, M. Cococcioni, D. A. Scherlis and N. Marzari, *Phys. Rev. Lett.*, 2006, **97**, 103001.

25 J. H. Jung, K. H. Kim, D. J. Eom, T. W. Noh, E. J. Choi, J. J. Yu, Y. S. Kwon and Y. Chung, *Phys. Rev. B: Condens. Matter Mater. Phys.*, 1997, **55**, 15489–15493.

26 J. Hong, A. Stroppa, J. Iniguez, S. Picozzi and D. Vanderbilt, *Phys. Rev. B: Condens. Matter Mater. Phys.*, 2012, **85**, 054417.

27 U. Aschauer, R. Pfenninger, S. M. Selbach, T. Grande and N. A. Spaldin, *Phys. Rev. B: Condens. Matter Mater. Phys.*, 2013, **88**, 054111.

28 P. E. Blochl, *Phys. Rev. B: Condens. Matter Mater. Phys.*, 1994, **50**, 17953–17979.

29 G. Kresse and D. Joubert, *Phys. Rev. B: Condens. Matter Mater. Phys.*, 1999, **59**, 1758–1775.

30 G. Kresse and J. Hafner, *Phys. Rev. B: Condens. Matter Mater. Phys.*, 1994, **49**, 14251–14269.

31 G. Kresse and J. Furthmuller, *Phys. Rev. B: Condens. Matter Mater. Phys.*, 1996, **54**, 11169–11186.

32 J. P. Perdew, K. Burke and M. Ernzerhof, *Phys. Rev. Lett.*, 1996, **77**, 3865–3868.

33 A. I. Liechtenstein, V. I. Anisimov and J. Zaanen, *Phys. Rev. B: Condens. Matter Mater. Phys.*, 1995, **52**, R5467–R5470.

14116 | *J. Mater. Chem. A*, 2014, **2**, 14109–14117

This journal is © The Royal Society of Chemistry 2014

34 E. Antonides, E. C. Janse and G. A. Sawatzky, *Phys. Rev. B: Condens. Matter Mater. Phys.*, 1977, **15**, 1669–1679.

35 V. I. Anisimov, J. Zaanen and O. K. Andersen, *Phys. Rev. B: Condens. Matter Mater. Phys.*, 1991, **44**, 943–954.

36 D. A. Tompsett, D. S. Middlemiss and M. S. Islam, *Phys. Rev. B: Condens. Matter Mater. Phys.*, 2012, **86**, 205126.

37 D. A. Tompsett, S. C. Parker, P. G. Bruce and M. S. Islam, *Chem. Mater.*, 2013, **25**, 536–541.

38 J. B. Goodenou, *Phys. Rev.*, 1967, **164**, 785–789.

39 P. Blaha, K. Schwarz, P. Sorantin and S. B. Trickey, *Comput. Phys. Commun.*, 1990, **59**, 399–415.

40 K. Schwarz, P. Blaha and G. K. H. Madsen, *Comput. Phys. Commun.*, 2002, **147**, 71–76.

41 W. Kohn and L. J. Sham, *Phys. Rev.*, 1965, **140**, 1133–1138.

42 G. K. H. Madsen and D. J. Singh, *Comput. Phys. Commun.*, 2006, **175**, 67–71.

43 A. Togo, F. Oba and I. Tanaka, *Phys. Rev. B: Condens. Matter Mater. Phys.*, 2008, **78**, 134106.

44 J. M. Skelton, S. C. Parker, A. Togo, I. Tanaka and A. Walsh, *Phys. Rev. B: Condens. Matter Mater. Phys.*, 2014, **89**, 205203.

45 K. Momma and F. Izumi, *J. Appl. Crystallogr.*, 2008, **41**, 653–658.

46 W. Paszkowicz, J. Pietosa, S. M. Woodley, P. A. Dluzewski, M. Kozlowski and C. Martin, *Powder Diffr.*, 2010, **25**, 46–59.

47 Q. Zhou and B. J. Kennedy, *J. Phys. Chem. Solids*, 2006, **67**, 1595–1598.

48 W. Paszkowicz, S. Woodley, P. Piszora, B. Bojanowski, J. Piętosa, Y. Cerenius, S. Carlson and C. Martin, *Appl. Phys. A*, 2013, 1–7.

49 N. N. Loshkareva and E. V. Mostovshchikova, *Phys. Met. Metallogr.*, 2012, **113**, 19–38.

50 E. O. Wollan and W. C. Koehler, *Phys. Rev.*, 1955, **100**, 545–563.

51 V. Markovich, I. Fita, A. Wisniewski, R. Puzniak, D. Mogilyansky, L. Titelman, L. Vradman, M. Herskowitz and G. Gorodetsky, *Phys. Rev. B: Condens. Matter Mater. Phys.*, 2008, **77**, 054410.

52 T. Nguyen Thuy, C. Bach Thanh, T. Pham Huong, T. Pham The, T. Nguyen Duc and N. Hoang Nam, *Phys. B*, 2011, **406**, 3613–3621.

53 N. Hamdad and B. Bouhafs, *Phys. B*, 2010, **405**, 4595–4606.

54 F. F. Fava, P. Darco, R. Orlando and R. Dovesi, *J. Phys.: Condens. Matter*, 1997, **9**, 489–498.

55 W. E. Pickett and D. J. Singh, *Phys. Rev. B: Condens. Matter Mater. Phys.*, 1996, **53**, 1146–1160.

56 W. Luo, A. Franceschetti, M. Varela, J. Tao, S. J. Pennycook and S. T. Pantelides, *Phys. Rev. Lett.*, 2007, **99**, 036402.

57 S. Bhattacharjee, E. Bousquet and P. Ghosez, *J. Phys.: Condens. Matter*, 2008, **20**, 255229.

58 S. Satpathy, Z. S. Popovic and F. R. Vukajlovic, *J. Appl. Phys.*, 1996, **79**, 4555–4557.

59 H. Tsukahara, S. Ishibashi and K. Terakura, *Phys. Rev. B: Condens. Matter Mater. Phys.*, 2010, **81**, 214108.

60 L. Rormark, A. B. Morch, K. Wiik, S. Stolen and T. Grande, *Chem. Mater.*, 2001, **13**, 4005–4013.

61 B. Dorado and P. Garcia, *Phys. Rev. B: Condens. Matter Mater. Phys.*, 2013, **87**, 195139.

62 Z. Zeng, M. Greenblatt and M. Croft, *Phys. Rev. B: Condens. Matter Mater. Phys.*, 1999, **59**, 8784–8788.

63 M. Molinari, S. C. Parker, D. C. Sayle and M. S. Islam, *J. Phys. Chem. C*, 2012, **116**, 7073–7082.

64 P. H. Klose, *J. Electrochem. Soc.*, 1970, **117**, 854–858.

65 R. Metselaar, R. E. J. Vantol and P. Piercy, *J. Solid State Chem.*, 1981, **38**, 335–341.

66 E.-S. Lee, S. Cho, H.-K. Lyeo and Y.-H. Kim, *Phys. Rev. Lett.*, 2014, **112**, 136601.

67 J. L. Cohn, C. Chiorescu and J. J. Neumeier, *Phys. Rev. B: Condens. Matter Mater. Phys.*, 2005, **72**, 024422.

68 D. S. Alfaruq, E. H. Otal, M. H. Aguirre, S. Populoh and A. Weidenkaff, *J. Mater. Res.*, 2012, **27**, 985–990.

69 J. Lan, Y. Lin, A. Mei, C. Nan, Y. Liu, B. Zhang and J. Li, *J. Mater. Sci. Technol.*, 2009, **25**, 535–538.

70 G. J. Xu, R. Funahashi, Q. R. Pu, B. Liu, R. H. Tao, G. S. Wang and Z. J. Ding, *Solid State Ionics*, 2004, **171**, 147–151.

71 D. Flahaut, T. Mihara, R. Funahashi, N. Nabeshima, K. Lee, H. Ohta and K. Koumoto, *J. Appl. Phys.*, 2006, **100**, 084911.

72 C.-J. Liu, A. Bhaskar and J. J. Yuan, *Appl. Phys. Lett.*, 2011, **98**, 214101.

73 J. L. Cohn, M. Peterca and J. J. Neumeier, *J. Appl. Phys.*, 2005, **97**, 034102.

74 P. Garcia-Fernandez, M. Verissimo-Alves, D. I. Bilc, P. Ghosez and J. Junquera, *Phys. Rev. B: Condens. Matter Mater. Phys.*, 2012, **86**, 085305.

75 M. Ohtaki, H. Koga, T. Tokunaga, K. Eguchi and H. Arai, *J. Solid State Chem.*, 1995, **120**, 105–111.